Research Article

Mechanism and Modeling of Contaminant Accumulation on Hot-Film Air Flow Sensor

Changrong Yuan [iD], **Zhongsheng Sun** [iD], **and Xiaoning Li**

School of Mechanical Engineering, Nanjing University of Science and Technology, Nanjing 210094, China

Correspondence should be addressed to Zhongsheng Sun; billsun1978@163.com

Hot-film air flow sensors are now widely applied in many industrial fields. Their accuracy can be seriously affected when there are contaminants accumulated on the sensor chip. To predict the decrease of accuracy caused by contamination, the accumulation mechanism of contaminant particles on the surface of the sensor chip is studied in this paper. The adsorption process of particle is analyzed and a theoretical model of the cumulative thickness of the particles over time is established. A test platform for the particle accumulation is built and a long-term cumulative test is conducted. According to the tests, cumulative thickness of the particles increases while the growth rate slows over time. The results of the test fit those of the theoretical model. Various factors affecting the accumulation of contaminants are analyzed. The results indicate that the cumulative thickness of the particles increases along with the increase of the particle concentration, the particle charge, and the electric field strength on the chip surface but decreases along with the increase of the particle radius. The test results also show that the electrical force is the dominant reason of particle adsorption accumulation. By decreasing the electric field strength on the sensor surface, the cumulative thickness of the particles can be effectively reduced.

1. Introduction

In recent years, MEMS hot-film air flow sensor has been widely used in the fields of aerospace, automotive, biomedical, environmental monitoring, semiconductor, and domestic appliances due to its ability of indirect measurement of air mass flow via measurements of temperature changes and the characteristics of high accuracy, fast response, and low power consumption [1–3]. However, in practical applications, it is found that if the gas to be measured contains aerosol particles, oil mist, etc., the surface of the sensor chip will be contaminated, which affects the accuracy of the sensor. For example, one of the typical applications of MEMS hot-film flow sensor is in the field of automotive engines [4–6]. It is an important sensor for controlling the air-fuel ratio in the electronic control fuel injection device of the automobile. It is used to measure the air flow inhaled into the engine as a basic signal for determining the fuel injection, which directly affects the performance of the power, cost, emission, and stable operation of the automobile engine [7]. As the automotive engine usually works in a dirty air environment,

the measurement area of the sensor would be contaminated by the prevalent pollutants [8, 9]. A heat insulating layer is generated to make the sensor difficult to dissipate, which would produce an air-fuel ratio error of 30%-45% [10]. When the sensor is contaminated, it would cause the problems such as difficulty in starting the engine, unstable idle speed, power reduction, and increased fuel consumption [11, 12].

Xu [13] used the Workbench Fluent module of ANSYS to analyze the flow field of the sensor chip in the presence of air contamination. It was found that the diameter of the particles and the amount of contaminants in the air are the main factors affecting the temperature distribution of the sensor chip. Komorska [14] studied the effect of partial choking on the intake manifold. The air cannot flow through the part of the channel blocked by the contaminants, which affects the distribution of the airflow over the entire channel area, thus causing the flow rate calculated by the sampling part to be out of alignment. Hecht et al. [15, 16] studied the effect of thermophoretic force on the accumulation of contaminants. The thermophoretic force was used to reduce the accumulation of tiny particles such as dust and oil
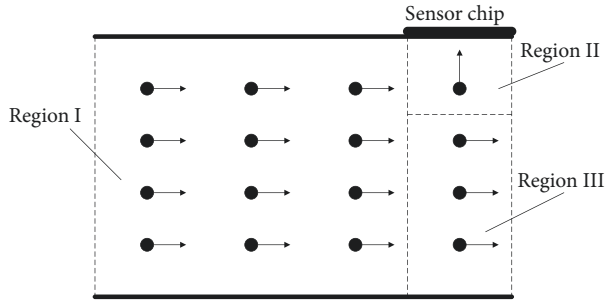
FIGURE 1: Schematic diagram of accumulation of contaminant particles on the surface of the chip.

FIGURE 2: Schematic diagram of the forces of particles in the pipe before approaching the surface of the chip. F_d: drag force; F_b: buoyancy; F_g: gravity; F_p: pressure gradient force; F_s: Saffman lift force; u_{gx}: velocity of the gas in x-axis direction.

mist by adding heating resistance on the surface of the hot film. In [17], the influence of electric field and sensor chip position on the accumulation of particles was studied through experiments. The results show that the accumulation of particles is exacerbated due to the presence of the electric field, and the gravity of the particles has no significant effect on the accumulation of particles.

As MEMS hot-film gas flow sensors have been widely used in the past decade, the problem of contamination in its application is just exposed, resulting in a lack of targeted research work. In addition, the sensor chip is relatively small, and the research of the contamination on the surface of the chip is difficult, so that there are few related literatures on practical operation. In this paper, the accumulation mechanism of contaminant particles on the surface of the sensor chip is studied. The particle motion is analyzed and a theoretical model of the cumulative thickness of the particles over time is established. The factors affecting the accumulation of particles are analyzed by the model. It is proposed to reduce the contaminants by decreasing the electrical force on the surface of the chip.

2. Accumulation Mechanism and Model

2.1. Analysis of Accumulation Mechanism of Contaminant Particles.
MEMS hot-film gas flow sensors are often used in harsh working environments where contaminants are contained. Contaminants can be accumulated on the surface of the sensor chip, affecting the accuracy of the sensor [18]. There are many forces that affect the accumulation of contaminant particles, such as air adhesion, air buoyancy, gravity of the particles themselves, Saffman lift force, electrical force, etc. [19, 20]. When the particles move inside the pipe, most of them get charged due to the collisions and frictions. Since an electric field is generated by the energized thin film resistors, the particles passing through the surface of the chip experience the electrical force. As the electric field decreases along with the increase of the distance, the influence of the electrical force on the particle accumulation also decreases along with the increase of the distance. Therefore, particles in a certain range of the flow channel above the surface of the chip will be accumulated by the electrical force generated on the chip surface, as shown in Figure 1. The particle motion is specifically considered in two stages: (1) the particles in the
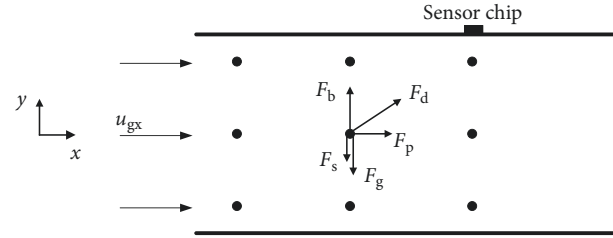
region I are transported horizontally in the pipe at a certain speed before entering the surface of the sensor chip, and the applied forces are in a balanced state; (2) when the particles flowing from the region I into the region II pass through the surface of the sensor chip, the original force balance of the particles is broken due to the new electrical force, resulting in the adsorption and accumulation on the surface of the chip. The particles far away from the surface of the chip (region III) are less affected by the electrical force and the particles will not be adsorbed.

2.2. Single Particle Adsorption Process Description

2.2.1. Basic Force and Motion Analysis of Particles in the Pipe.
The contaminant particles in the pipe experience the basic force and motion [21, 22] before being affected by the electrical force on the surface of the chip. The flow process can be approximately described by a free and uniform suspension flow model that ignores the friction and collision between particles and between the particles and the pipe, and studies the motion discipline of single particle to investigate the situation of the entire flow channel. The particles moving in the horizontal pipe are mainly forced by drag force F_d of the gas to the particles, buoyancy F_b, gravity F_g, pressure gradient force F_p, and Saffman lift force F_s, as shown in Figure 2. In the horizontal direction, the particles move forward along the pipe for a long time or distance, reach a certain final velocity, and then maintain a uniform motion by the horizontal component force F_{dx} of drag force F_d and pressure gradient force F_p. In the vertical direction, the particles are transported in suspension by the vertical component force F_{dy} of drag force F_d, buoyancy F_b, gravity F_g, and Saffman lift force F_s.

According to Newton's second law, in the x-axis direction, the particles experience the horizontal component force F_{dx} of drag force and pressure gradient force F_p, which can be expressed as

$$m_p \frac{du_{px}}{dt} = F_{dx} + F_p \tag{1}$$

In the y-axis direction, the particles are under the vertical component force F_{dy} of drag force, buoyancy F_b, gravity F_g, and Saffman lift force F_s, which can be given by

$$m_p \frac{du_{py}}{dt} = F_{dy} + F_b - F_g - F_s \quad (2)$$

The expressions of drag force F_d, buoyancy F_b, gravity F_g, pressure gradient force F_p, and Saffman lift force F_s [19, 23] are substituted into (1) and (2):

$$m_p \frac{du_{px}}{dt} = 6\pi\mu r_p \left(u_{gx} - u_{px}\right) - V_p \frac{\partial p}{\partial x} \quad (3)$$

$$m_p \frac{du_{py}}{dt} = 6\pi\mu r_p \left(u_{gy} - u_{py}\right) + \rho_g g V_p - m_p g$$
$$- 6.44 \left(\mu\rho_g\right)^{1/2} r_p^2 \left(u_{gx} - u_{px}\right) \left|\frac{du_{gx}}{dy}\right|^{1/2} \quad (4)$$

where m_p is the mass of particle, u_{px} is the velocity of particle in the x-axis direction, μ is the aerodynamic viscosity coefficient, r_p is the radius of particle, u_{gx} is the velocity of gas in the x-axis direction, V_p is the volume of particle, p is the pressure in the flow channel, u_{py} is the velocity of particle in the y-axis direction, u_{gy} is the velocity of gas in the y-axis direction, ρ_g is the density of gas, and g is gravity acceleration.

In the x-axis direction, when the particles are accelerated to the maximum speed, the horizontal acceleration will be 0 and the particles maintain a constant velocity:

$$\frac{du_{px}}{dt} = 0 \quad (5)$$

Substituting (5) into (3)

$$6\pi\mu r_p \left(u_{gx} - u_{px}\right) - V_p \frac{\partial p}{\partial x} = 0 \quad (6)$$

In the y-axis direction, when the particles are in equilibrium state, the vertical acceleration is 0:

$$\frac{du_{py}}{dt} = 0 \quad (7)$$

Substituting (7) into (4)

$$6\pi\mu r_p \left(u_{gy} - u_{py}\right) + \rho_g g V_p - m_p g$$
$$- 6.44 \left(\mu\rho_g\right)^{1/2} r_p^2 \left(u_{gx} - u_{px}\right) \left|\frac{du_{gx}}{dy}\right|^{1/2} = 0 \quad (8)$$

The particles move in the pipe for a long time and gradually reach a steady state. u_{px} and u_{py} in (6) and (8) are the x-direction and y-direction velocity when the contaminant particles reach the steady state and also are the initial velocity of particles entering the sensor chip.

2.2.2. Force and Motion Analysis of Particles Adsorbed on the Surface of the Chip. When the particles move inside the pipe, most of them get charged due to the collisions and frictions [24]. The charged particles additionally experience the electrical force from the sensor chip and the adhesion resistance from the gas. The electric field strength around

the chip decreases along with the increase of distance, so most of the particles far away from the surface of the chip move normally in the pipe. Only the charged particles close to the chip are adsorbed by the electrical force generated on the sensor chip to overcome the gas adhesion resistance and accumulate on the surface of the chip. Particles far away from the surface of the chip are still forced by F_d, F_b, F_g, F_p, and F_s and flow horizontally along the pipe. The charged particles near the surface of the chip are affected by the electrical force F_e and the gas adhesion resistance F_r in addition to the effects of F_d, F_b, F_g, F_p, and F_s, as shown in Figure 3. The electrical force F_e causes the particles to accumulate on the surface of the chip, and the adhesion resistance F_r prevents the particles from moving toward the surface of the chip.

The hot-film flow sensor consists of a heating resistor, an upstream temperature measuring resistor and a downstream temperature measuring resistor. When the sensor is energized, an electric field is generated around the heating resistor and the temperature measuring resistors in the middle of the chip. The heating resistor and the temperature measuring resistors are fabricated on the chip surface with the metal arrays. Although the total lateral extension of the metal arrays is significantly larger than those of the particles passing by, the width of a single metal wire (lateral extension) is small (only a few microns), which is similar to the particle size. So the electric field of a uniformly charged line source is utilized to estimate the electric force acting on the particles passing by. Assuming that the charge line density is λ_e and the particle charge is q_p, the electrical force F_e of the charged particles [25] is expressed as

$$F_e = \frac{q_p \lambda_e}{2\pi\varepsilon_0 \left(R - y\right)} \quad (9)$$

where ε_0 is the vacuum dielectric constant and R is the radius of pipe.

The particles additionally experience the adhesion resistance of the gas when they are adsorbed to the surface of the chip [26], which can be given by

$$F_r = \frac{\pi r_p^2}{2} C_D \rho_g u_{px}^2 \quad (10)$$

where C_D is the coefficient of resistance.

According to Newton's second law, in the x-axis direction, the particles still experience the horizontal component force F_{dx} of drag force and pressure gradient force F_p, which can be expressed as

$$m_p \frac{du_{px}}{dt} = F_{dx} + F_p \quad (11)$$

In the y-axis direction, the particles experience the electrical force F_e, adhesion resistance F_r, the vertical component force F_{dy} of drag force and Saffman lift force F_s, buoyancy F_b, and gravity F_g are ignored [17], which can be given by

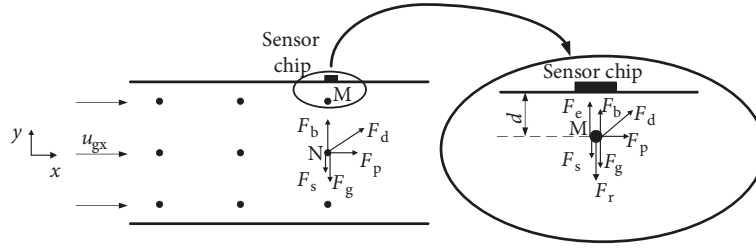$$m_p \frac{du_{py}}{dt} = F_e - F_r + F_{dy} - F_s \quad (12)$$

FIGURE 3: Schematic diagram of the forces when the particles are adsorbed to the surface of the chip. F_d: drag force; F_b: buoyancy; F_g: gravity; F_p: pressure gradient force; F_s: Saffman lift force; F_e: electrical force; F_r: adhesion resistance; d: distance between particle and chip; u_{gx}: velocity of the gas in x-axis direction.
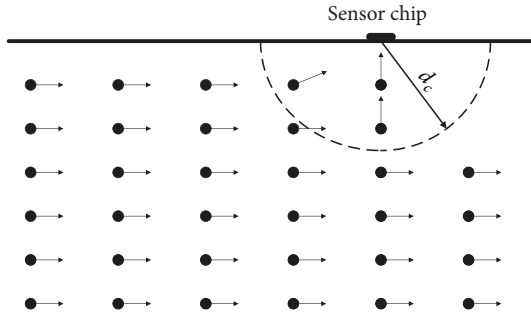

FIGURE 4: Schematic diagram of particles adsorbed to the surface of the chip.

The expressions of drag force F_d, pressure gradient force F_p, electrical force F_e, adhesion resistance F_r, and Saffman lift force F_s are substituted into (11) and (12):

$$m_p \frac{du_{px}}{dt} = 6\pi\mu r_p \left(u_{gx} - u_{px} \right) - V_p \frac{\partial p}{\partial x} \tag{13}$$

$$m_p \frac{du_{py}}{dt} = \frac{q_p \lambda_e}{2\pi\varepsilon_0 \left(R - y \right)} - \frac{\pi r_p^2}{2} C_D \rho_g u_{px}^2$$

$$+ 6\pi\mu r_p \left(u_{gy} - u_{py} \right) \tag{14}$$

$$- 6.44 \left(\mu\rho_g \right)^{1/2} r_p^2 \left(u_{gx} - u_{px} \right) \left| \frac{du_{gx}}{dy} \right|^{1/2}$$

The charged particles near the chip can be adsorbed on the surface of the chip in the situation that the resultant force of the electrical force and the vertical component force of drag force must be greater than or equal to the resultant force of the adhesion resistance and the Saffman lift force. The equation can be given by

$$F_e + F_{dy} \geq F_r + F_s \tag{15}$$

The electrical force of the particles increases along with the decrease of the distance. When the distance between the particle and the surface of the chip is less than a certain value, $F_e + F_{dy} > F_r + F_s$, the particle accelerates toward the surface of the chip. When the distance between the particle and the surface of the chip is larger than a certain value, $F_e + F_{dy} <$

$F_r + F_s$, the particle cannot be adsorbed on the surface of the chip. Therefore, a critical distance d_c exists at which the particle will be absorbed to the surface of the chip when the distance between the particle and the chip is less than the critical distance; otherwise, the particle will not be adsorbed, as shown in Figure 4.

The force equation of the particles at the critical distance d_c can be considered as

$$F_{ec} + F_{dy} = F_r + F_s \tag{16}$$

where F_{ec} is the electrical force of the particles at the critical distance d_c.

The expressions of electrical force F_e, the vertical component force F_{dy} of drag force, adhesion resistance F_r, and Saffman lift force F_s are substituted into (16):

$$\frac{q_p \lambda_e}{2\pi\varepsilon_0 d_c} + 6\pi\mu r_p \left(u_{gy} - u_{py} \right)$$

$$= \frac{\pi r_p^2}{2} C_D \rho_g u_{px}^2 \tag{17}$$

$$+ 6.44 \left(\mu\rho_g \right)^{1/2} r_p^2 \left(u_{gx} - u_{px} \right) \left| \frac{du_{gx}}{dy} \right|^{1/2}$$

where d_c is the critical distance between the particle and the surface of the chip.

2.3. Mathematical Model of Accumulation of Particles on Sensor Chip. The charged particles can be adsorbed and accumulated within the critical distance d_c from the chip surface (o' point) when they move in the pipe, as shown in Figure 5. They will be adsorbed by the electric field in the range of arc 'MGN'. It means that the charged particles passing through arc 'MGN' will be adsorbed in the x-o-y plane. Seen from the z-o-y plane, the particles in the rectangular 'ABCD' will be adsorbed to accumulate on the surface of the chip.

The total mass of charged particles that can be adsorbed to the surface of the chip during time t is as follows [27]:

$$M_{all} = \eta\psi V_{all} = \eta\psi l_r d_c \overline{u_{px}} t \tag{18}$$

where η is the proportion of unipolar charged particles, Ψ is the average mass concentration of particles, l_r is the length
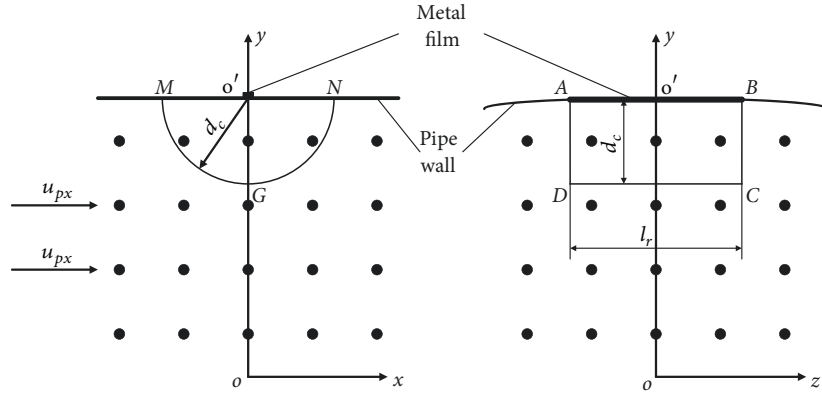
FIGURE 5: Schematic diagram of range of particles absorbed to the surface of the chip.
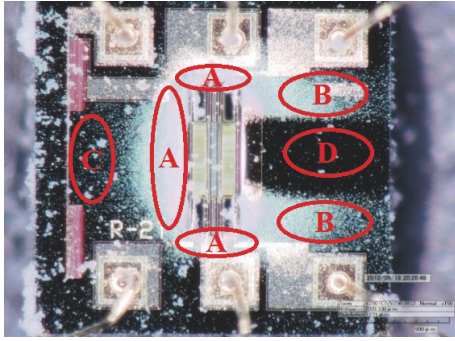

FIGURE 6: Physical diagram of contaminant particles accumulated on the surface of the chip.

of charged straight line, and $\overline{u_{px}}$ is the average velocity of the particles in the area 'ABCD'.

The velocity of the particles in the x-axis direction is solved by (6). Following from the Hagen–Poiseuille equation, $\partial p / \partial x$ and u_{gx} can be given by

$$\frac{\partial p}{\partial x} = \frac{\Delta p}{L} = \frac{8\mu q_v}{\pi R^4} \tag{19}$$

$$u_{gx} = \frac{\Delta p}{4\mu L}\left(R^2 - y^2\right) = \frac{2q_v}{\pi R^4}\left(R^2 - y^2\right) \tag{20}$$

where Δp is the gas pressure difference, q_v is the volumetric flow rate, and L is the length of pipe.

Therefore, the expression of the particle velocity in the x-axis direction is as follows:

$$u_{px} = u_{gx} - \frac{V_p}{6\pi\mu r_p}\frac{\partial p}{\partial x} = \frac{2q_v}{\pi R^4}\left(R^2 - y^2\right) - \frac{4q_v V_p}{3\pi^2 R^4 r_p} \tag{21}$$

The average particle velocity in the area 'ABCD' is given by

$$\overline{u_{px}} = \frac{1}{d_c}\int_{R-d_c}^{R} u_{px}dy$$

$$= \frac{q_v}{\pi R^4}\left(-\frac{2}{3}d_c^2 + 2Rd_c - \frac{16}{9}r_p^2\right) \tag{22}$$

Substituting (22) into (18), the expression of M_{all} is

$$M_{all} = \eta\psi l_r d_c \overline{u_{px}} t$$

$$= \frac{\eta\psi l_r q_v t}{\pi R^4}\left(-\frac{2}{3}d_c^3 + 2Rd_c^2 - \frac{16}{9}r_p^2 d_c\right) \tag{23}$$

A regularity is formed in the process of particle accumulation on the surface of the chip. The charged particles are mainly accumulated around the central region (the thin film resistance arrangement region) and keep a 'U'-shaped distribution due to the electric field generated around the thin film resistor, as shown in Figure 6. As the electric field in the edges of the electrodes is significantly increased, the cumulative thickness of the particles in the edge of the thin film resistor is larger than that in the middle of the thin film resistor in region A. The cumulative thickness of the particles in regions B, C, and D can be ignored because it is much smaller than that in region A. Assuming that the particles are equal-diameter spheres and the particles are accumulated regularly on the surface of the chip with positive italic rule. The cumulative state diagram is shown in Figure 7.

The number of A-A cross-section particles is

$$N = i + i - 1 + \cdots + i - (j-1) = ij - \frac{1}{2}j^2 + \frac{1}{2}j \tag{24}$$

The geometric relationship is

$$h_t = 2r_p j \sin\theta \tag{25}$$

$$b = a + 2h_t \cot\theta = 2r_p i \tag{26}$$

Then the total number of particles accumulated on the surface of the chip is

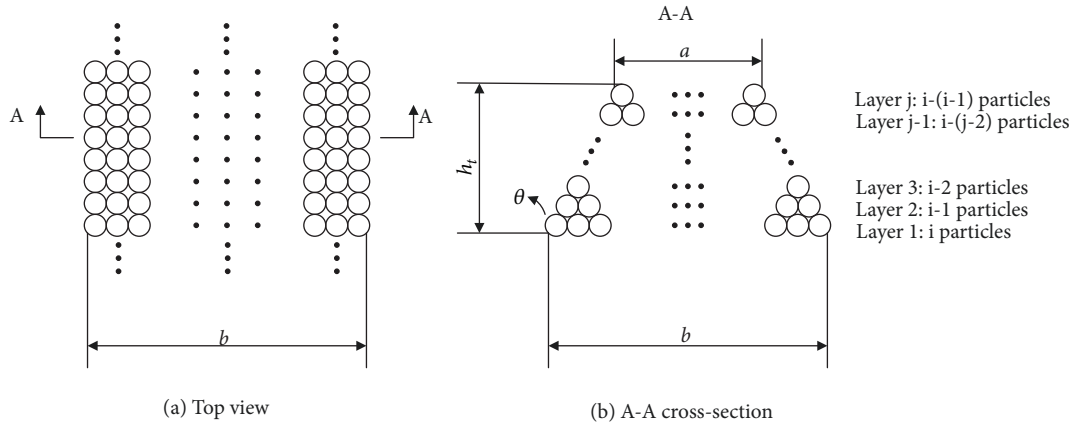(a) Top view   (b) A-A cross-section

FIGURE 7: Schematic diagram of the accumulation state of contaminant particles on the surface.

$$N_{all} = \frac{l_p}{2r_p}N$$
$$= \frac{l_p}{2r_p}\left(\frac{ah_t + 2h_t^2\cot\theta}{4r_p^2\sin\theta} - \frac{h_t^2}{8r_p^2\sin^2\theta} + \frac{h_t}{4r_p\sin\theta}\right) \quad (27)$$

where N is the number of A-A cross-section particles, l_p is the particle 'U'-shaped cumulative length, θ is the bottom angle, a, b are the side lengths, and h_t is the cumulative thickness of the particles over time.

According to the qualitative relationship of the particles themselves, the total number of particles (N_{all}) can also be expressed as

$$N_{all} = \frac{M_{all}}{\rho_p V_p} \quad (28)$$

Substituting (27) into (28)

$$h_t^2 + \frac{\left(2a\sin\theta + 2r_p\sin\theta\right)}{4\cos\theta - 1}h_t - \frac{16M_{all}r_p^3\sin^2\theta}{(4\cos\theta - 1)l_p\rho_p V_p} \quad (29)$$
$$= 0$$

Solving (29)

$$h_t = \sqrt{\frac{12M_{all}\sin^2\theta}{(4\cos\theta - 1)\pi l_p\rho_p} + \frac{\left(a + r_p\right)^2\sin^2\theta}{(4\cos\theta - 1)^2}}$$
$$- \frac{\left(a + r_p\right)\sin\theta}{4\cos\theta - 1} \quad (30)$$

Substituting (23) into (30)

$$h_t = \sqrt{\frac{12\eta\psi l_r q_v t\left(-(2/3)d_c^3 + 2Rd_c^2 - (16/9)r_p^2 d_c\right)\sin^2\theta}{(4\cos\theta - 1)\pi^2 l_p\rho_p R^4} + \frac{\left(a + r_p\right)^2\sin^2\theta}{(4\cos\theta - 1)^2}} - \frac{\left(a + r_p\right)\sin\theta}{4\cos\theta - 1} \quad (31)$$

3. Basic Test of Adsorption Accumulation and Reverse Calculation of Electric Parameter

3.1. Test Scheme and Platform

3.1.1. Microsilicon Powder Test. In order to study the cause of the accumulation of tiny particles on the surface of the MEMS flow sensor chip, the contamination environment was simulated and the microsilicon powder test scheme was designed. The test was divided into Scheme I and Scheme II, as shown in Table 1. In Scheme I, the No.1 sensor was energized while the No.2 sensor was not energized to compare the effect of energization on the accumulation of contaminant particles. In Scheme II, the chip of No.1 sensor was located at the top of the pipe, while the chip of No.3 sensor

was located at the bottom of the pipe, to study the effect of chip position on the accumulation of contaminant particles.

The test circuit diagram and the physical diagram are shown in Figure 8. The throttle valves 10, 11, and 12 are adjusted to control the flow through the sensor. The throttle valve 4 is adjusted to control the flow through the powder generator 7, thereby controlling the concentration of microsilica powder in the gas. The microsilica powder passes through the test sensors after being fully mixed with the gas in the mixing chamber 9. The concentration of the microsilicon powder is detected by an aerosol particle monitor 18 manufactured by TSI Company of the United States with model number DUST-TRAKTM II. During the test, the gas supply pressure is 0.1 MPa.

TABLE 1: MEMS hot-film flow sensor contaminant accumulation test scheme.

Scheme number	Test purpose	Sensor number	Scheme description	Test parameter	
				Flow(L/min)	Test medium
I	Testing the effect of energization on contaminant accumulation	1	Energized		
		2	No energized		
II	Testing the effect of chip position on contaminant accumulation	1	Chip located at the top	0.8	Air-micro-silica two-phase flow
		3	Chip located at the bottom		

TABLE 2: Different filtration accuracy test scheme.

Test purpose	Sensor number	Scheme description	Test parameter	
			Flow(L/min)	Test medium
Testing the effect of filtration accuracy on contaminant accumulation	4	High-accuracy filter		Clean air (0.01μm)
	5	Low-accuracy filter	0.8	Normal air (5.0μm)

The particles accumulated on the surface of the chip are generally considered to be measured by the laser due to their microsizes. Although the laser can measure the height of the contaminants, the overall morphology of the contaminants cannot be observed. After investigation, the digital microscope VHX-1000 of Keyence is finally used for the measurement. This microscope can achieve both 2D and 3D images. The distribution and cumulative thickness of microsilica particles on the surface of MEMS flow sensor chip can be shown clearly by the microscope.

3.1.2. Air Test. To study the trend of the flow sensor accuracy over time under different filtration accuracy conditions, the sensors were tested with only air and monitored for a long time. The flow rates of the sensor and the morphology characteristics of the chip surface were compared by setting the filters with different filtration levels. The test scheme is shown in Table 2. The test circuit diagram and the physical diagram are shown in Figure 9. A high-accuracy filter is attached in the front of the No.4 sensor, the model number is SFD100 and the filtration level is 0.01 μm. The filter used in the front of the No.5 sensor comes from the pneumatic modular FRL (air filter, regulator, and lubricator), the model number is AF60, and the filtration level is 5.0 μm.

3.2. Test Results

3.2.1. Microsilica Powder Test Results. The test was carried out for a total of 180 hours. The flow rate of the sensor and the cumulative thickness of the microsilica powder on the chip surface were measured at 60h, 120h, and 180h, respectively. The values are shown in Table 3. The cumulative thickness of microsilica powder measured by the digital microscope is shown in Figure 10. As can be seen from Table 3, when the sensors are tested for 180 hours, the flow rate of No.1 sensor which is energized declines by 6.5 L/min compared to the reference flow rate of 15 L/min, and the decrease

amplitude is 43.333%. The flow rate of No.2 sensor which is not energized declines by 1.5 L/min compared to the reference flow rate of 15 L/min, and the decrease amplitude is 10%. The flow rate of No.3 sensor which is placed opposite to No.1 sensor declines by 5.7 L/min compared to the reference flow rate of 15 L/min, and the decrease amplitude is 38%. The cumulative thickness of the particles on the chip surface of No.1 sensor is 42.864 μm, No.2 sensor is 12.343 μm, and No.3 sensor is 39.801 μm, respectively. The decrease amplitude of flow rate and the cumulative thickness of the particles on No.1 sensor are approximately four times that of No.2 sensor. The particles are accumulated around the central region (the thin film resistance arrangement region) of the chip surface when the sensor is energized, while the particles are irregularly accumulated and relatively few when the sensor is not energized. These results show that the accumulation of contaminant particles significantly increases under energization, which indicates that an electric field is generated on the sensor chip and exacerbates particle adsorption. The differences of the decrease amplitude of the flow rate and the cumulative thickness of the particles between No.1 sensor and No.3 sensor are negligible. It shows that the gravity of the particles has a little effect on the accumulation of the particles.

3.2.2. Air Test Results. The test was carried out for a total of 195 days. The flow rate of the sensor and the morphology on the chip surface were measured at 39 days and 195 days, respectively. The values are shown in Table 4. The cumulative thickness of contaminants measured by the digital microscope is shown in Figure 11. As can be seen from Table 4, when the sensors are tested for 195 days, the flow rate of No.4 sensor with high-accuracy filter does not decrease compared to the reference flow rate of 15 L/min. The flow rate of No.5 sensor with low-accuracy filter declines by 0.3 L/min compared to the reference flow rate of 15 L/min, and the decrease amplitude is 2%. There is no obvious

TABLE 3: Flow rate measured by No.1~No.3 sensors and cumulative thickness of particles on chip surface.

Test time (h)	Sensor flow rate(L/min)				Particle cumulative thickness(μm)		
	Ref.	No.1	No.2	No.3	No.1	No.2	No.3
60	15	11.8	14.6	12.3	25.893	3.086	19.526
120	15	10.2	14.0	11.4	33.997	7.026	27.742
180	15	8.5	13.5	9.3	42.864	12.343	39.801
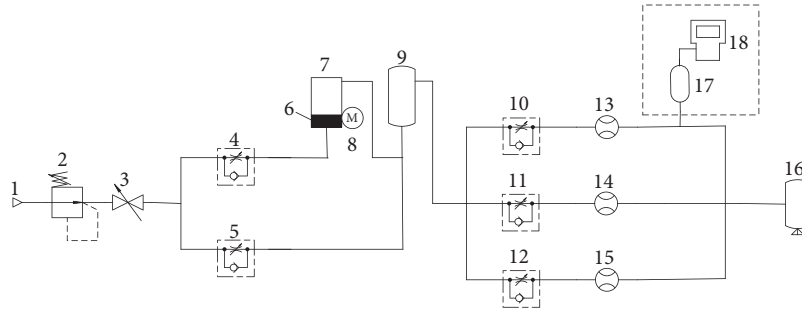
(a) Circuit diagram
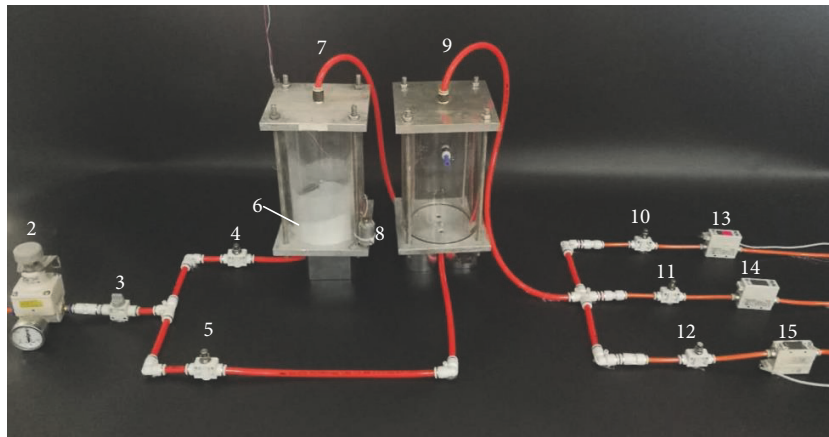
(b) Physical diagram

FIGURE 8: Circuit and physical diagram of microsilicon powder test. 1: air source; 2: regulator; 3: ball valve; 4, 5, 10, 11, and 12: Throttle valves; 6: microsilica powder; 7: powder generator; 8: motor; 9: mixing chamber; 13, 14, and 15: No.1, No.2, and No.3 sensors; 16: powder recycling; 17: gas tank; 18: aerosol particle monitor.

TABLE 4: Flow rate measured by No.4 and No.5 sensors and cumulative thickness of contaminants on chip surface.

Test time (day)	Sensor flow rate(L/min)			Particle cumulative thickness(μm)	
	Ref.	No.4	No.5	No.4	No.5
39	15	15	14.9	0	1.323
195	15	15	14.7	0	2.325

abnormality on the surface of No.4 sensor, while the oil mist is accumulated on the surface of No.5 sensor and the cumulative thickness is 2.325μm. The results show that the oil mist in the air is easily adsorbed on the surface of the sensor chip which do not pass through the high-accuracy filter. It illustrates that the sensors using high-accuracy filters can be

uncontaminated and the accuracy will remain stable for a long time.

3.3. *Reverse Calculation of Electric Parameter.* It can be known from (31) that the cumulative thickness h_t of the contaminant particles on the surface of the MEMS hot-film gas flow sensor chip is related to the critical distance d_c. The critical distance d_c can be solved by (17), where the electric parameter λ_e (the charge line density) is unknown. Due to the fact that the structure of the thin film resistance on the chip surface is quite complex and the size is small, the electric parameter is difficult to measure directly or calculate theoretically. Therefore, it is necessary to reversely calculate the line density λ_e based on the data measured by the basic test. When the contaminant particles enter the surface of the chip, the velocity of the gas and the particle in the x-direction
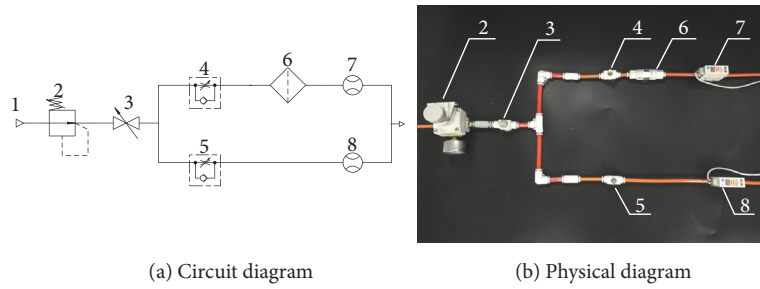
(a) Circuit diagram

(b) Physical diagram

Figure 9: Circuit and physical diagram of air test. 1: air source; 2: regulator; 3: ball valve; 4 and 5: Throttle valves; 6: high-accuracy filter; 7 and 8: No.4 and No.5 sensors.

(a) 60h(25.893μm)

(b) 120h(33.997μm)

(c) 180h(42.864μm)

(1) No.1 sensor cumulative thickness

(a) 60h(3.086μm)

(b) 120h(7.026μm)

(c) 180h(12.343μm)

(2) No.2 sensor cumulative thickness

(a) 60h(19.526μm)

(b) 120h(27.742μm)

(c) 180h(39.801μm)
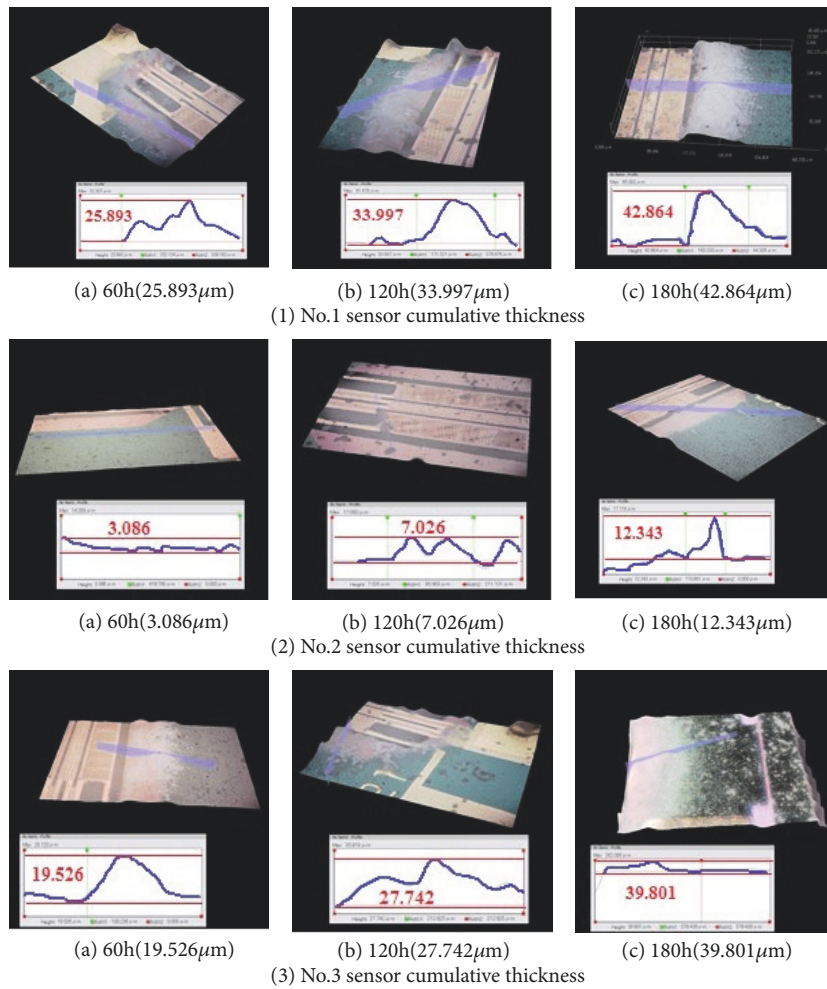
(3) No.3 sensor cumulative thickness

Figure 10: Cumulative thickness diagram of microsilicon powder on No.1~No.3 sensors.

are shown in (20) and (21), respectively. And the velocity in the y-direction is approximately zero. The expression of the charge line density λ_e can be obtained by substituting (20) and (21) into the (17):

$$\lambda_e = -\frac{24\pi\mu r_p q_v \varepsilon_0 d_c^3}{q_p R^4} + \frac{48\pi\mu r_p q_v \varepsilon_0 d_c^2}{q_p R^3}$$

$$+ 45.787 \frac{q_v r_p^4 \varepsilon_0 d_c}{R^6 q_p} \sqrt{\frac{\mu \rho_g q_v (R - d_c)}{\pi}}$$

$$- \frac{64\pi\mu q_v r_p^3 \varepsilon_0 d_c}{3 q_p R^4}$$

(32)

(a) 39d(0μm) (b) 195d(0μm)
(1) No.4 sensor morphology diagram

(a) 39d (b) 195d
(2) No.5 sensor morphology diagram

(a) 39d(1.323μm) (b) 195d(2.325μm)
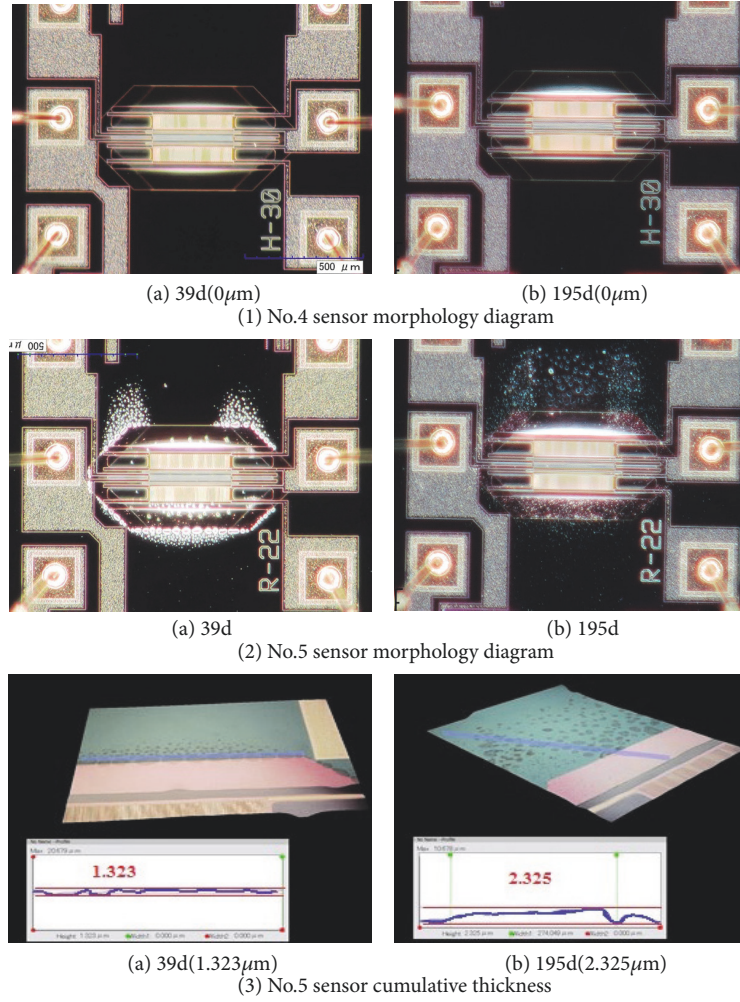(3) No.5 sensor cumulative thickness

FIGURE 11: Morphology and cumulative thickness diagram on No.4 and No.5 sensors.

After the charge line density λ_e is calculated by the experimental data, it can be used as a constant and substituted into (17) to obtain the solution equation of d_c:

$$\frac{12\mu r_p q_v d_c^3}{R^4} - \frac{24\mu r_p q_v d_c^2}{R^3}$$
$$- 22.893 \frac{q_v r_p^4 d_c}{\pi R^6} \sqrt{\frac{\mu \rho_g q_v (R - d_c)}{\pi}} + \frac{32\mu q_v r_p^3 d_c}{3R^4} \quad (33)$$
$$+ \frac{q_p \lambda_e}{2\pi\varepsilon_0} = 0$$

The values of the parameters in (31), (32), and (33) are shown in Table 5. The charge q_p and the proportion η of the microsilica particles are measured by the Millikan method [28]. The particle diameter is measured by a laser particle size analyzer with model number Mastersizer 2000. The concentration of the microsilicon powder is detected by an aerosol particle monitor with model number DUSTTRAKTM II. The side length a is approximately 0 as it is much smaller than the length b. The particle 'U'-shaped cumulative length and

TABLE 5: Parameter values in the theoretical formula.

Parameter	Value	Unit
q_p	6.4×10^{-17}	C
η	0.22	
d_p	3.311	μm
Ψ	5×10^{-6}	kg/m^3
a	0	m
l_p	1.2×10^{-3}	m
l_r	8×10^{-4}	m
ε_0	8.85×10^{-12}	F/m
μ	17.9×10^{-6}	Pas
ρ_g	1.21	kg/m^3
ρ_p	360	kg/m^3
R	4×10^{-3}	m
θ	60	°

the length of charged straight line are measured by the digital microscope VHX-1000 of Keyence. Other parameter values are constant.

TABLE 6: Value of d_c and λ_e calculated by the accumulation test of No.1 sensor.

Test time (h)	Cumulative thickness on No.1 sensor(μm)	Value of d_c based on Eq. (31)(μm)	Value of λ_e based on Eq. (32)(C/m)
60	25.893	66.893	5.706×10^{-10}
120	33.997	61.351	4.803×10^{-10}
180	42.864	62.651	5.008×10^{-10}

TABLE 7: Theoretical model verification test scheme for contaminant accumulation.

Test purpose	Sensor number	Scheme description	Flow (L/min)	Test parameter Concentration of micro-silica (μg/m^3)	Test medium
Verifying the correctness of theoretical model	6	Energized, chip located at the top	1	100	Air-micro-silica two-phase flow
	7		5	200	

TABLE 8: Flow rate measured by No.6 and No.7 sensors.

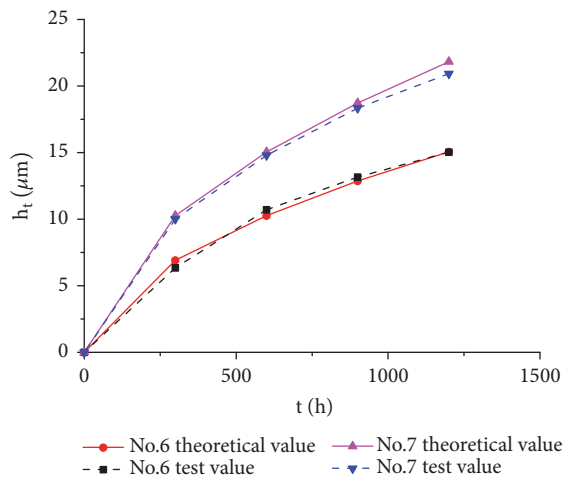| Test time (h)	Reference value (L/min)	No.6 sensor Flow rate (L/min)	No.6 sensor Decrease amplitude of accuracy (%)	No.7 sensor Flow rate (L/min)	No.7 sensor Decrease amplitude of accuracy (%)
300	15	14.4	4%	14.0	6.667%
600	15	13.9	7.333%	13.3	11.333%
900	15	13.6	9.333%	12.6	16%
1200	15	13.2	12%	11.9	20.667%

FIGURE 12: Comparison diagram of theoretical and test values of cumulative thickness on No.6 and No.7 sensors.

Taking microsilica powder accumulation test of No.1 sensor as an example, the critical distance d_c can be calculated by (31) based on the cumulative thickness of the particles measured at 60h, 120h, and 180h, respectively. The data is shown in Table 6. Then, the corresponding value of the charge line density λ_e is solved by (32). As a result, the average value of the charge line density λ_e is 5.172×10^{-10} C/m.

4. Verification Test and Analysis of Contaminant Accumulation Model

4.1. Verification Test and Result. In order to verify the correctness of the theoretical model, the atmospheric mild contamination test was simulated. The concentration of the microsilica powder was adjusted to 100 μg/m^3 and 200 μg/m^3, respectively. The test scheme is shown in Table 7. In this test, the cumulative thickness of the particles on the surface of the chip was tested every 300 hours, and a total of four cycles were tested. The flow rates measured by the sensors at different time are shown in Table 8. As can be seen from Table 8, when the sensors are tested for 1200 hours, the flow rate of No.6 sensor declines by 1.8 L/min compared to the reference flow rate of 15 L/min, and the decrease amplitude is 12%. The flow rate of No.7 sensor declines by 3.1 L/min compared to the reference flow rate of 15 L/min, and the decrease amplitude is 20.667%. When the gas flow rates are 1 L/min and 5 L/min, respectively, the values of the critical distance d_c can be calculated based on (33) to be 56.922 μm and 25.406 μm. The theoretical values of the cumulative thickness of the microsilica powder on the surface of the sensor chip at different time can be calculated by substituting the d_c value into (31). The theoretical calculation values and test measurement values of the cumulative thickness of the microsilica powder on No.6 and No.7 sensors at different time are shown in Table 9. The comparison diagram is shown in
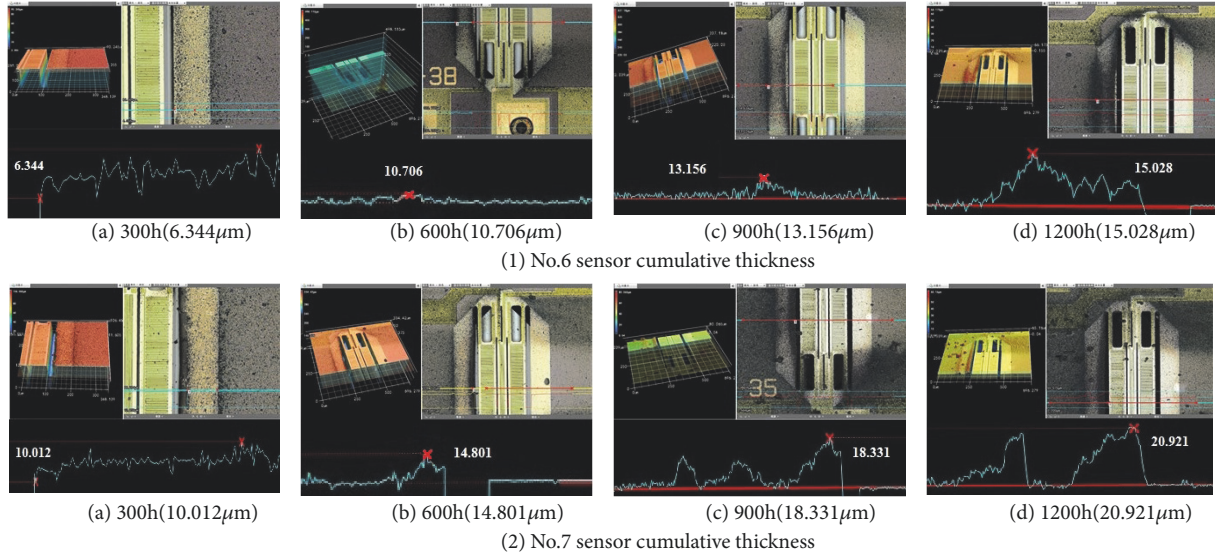
FIGURE 13: Cumulative thickness diagram of microsilicon powder on No.6 and No.7 sensors.

TABLE 9: Theoretical and test values of cumulative thickness on No.6 and No.7 sensors.

Test time	Cumulative thickness on No.6 sensor(μm)		Cumulative thickness on No.7 sensor(μm)	
(h)	Theoretical value	Test value	Theoretical value	Test value
300	6.905	6.344	10.263	10.012
600	10.272	10.706	15.046	14.801
900	12.867	13.156	18.724	18.331
1200	15.058	15.028	21.828	20.921

Figure 12. The cumulative thickness of microsilica powder measured by the digital microscope is shown in Figure 13. After 1200-hour test, the cumulative thickness of particles on the surface of No.6 sensor chip is 15.028μm, while that of No.7 sensor is 20.921μm. It can be seen from Figure 12 that the theoretical values of the cumulative thickness on the surface of No.6 sensor and No.7 sensor chip are in good agreement with the test values.

4.2. Analysis of Factors Affecting Accumulation. According to (31), the cumulative thickness of particles on the surface of the sensor chip is mainly related to the particle concentration Ψ, the particle radius r_p, and the critical distance d_c. The critical distance d_c can be calculated by (33). It can be seen from (33) that the critical distance d_c is related to the particle radius r_p, the particle charge q_p, and the chip surface charge line density λ_e. Therefore, the particle concentration Ψ, the particle radius r_p, the particle charge q_p, and the chip surface charge line density λ_e are the major factors affecting particle accumulation. When the gas flow rate is 1 L/min, the effects of various factors on the cumulative thickness of the particles are shown in Figure 14. As can be seen from Figures 14(a), 14(c), and 14(d), the cumulative thickness of the particles increases along with the increase of the particle concentration, the particle charge, and the chip

surface charge line density. After 100 hours of accumulation, the cumulative thickness increases from 8.655μm to 12.571μm when the particle concentration increases from 0.5mg/m^3 to 1mg/m^3, and the increase amplitude is 45.246%. The cumulative thickness increases from 12.571μm to 18.127μm when the particle charge increases from 1.6×10^{-17}C to 3.2×10^{-17}C, and the increase amplitude is 44.197%. The cumulative thickness increases from 29.176μm to 41.652μm when the chip surface charge line density increases from 5×10^{-9}C/m to 1×10^{-8}C/m, and the increase amplitude is 42.761%. Figure 14(b) shows that the cumulative thickness of the particles decreases along with the increase of the particle radius. After 100 hours of accumulation, the cumulative thickness decreases from 7.902μm to 4.079μm when the particle radius increases from 2μm to 4μm, and the decrease amplitude is 48.380%. The reason for the decline is that the larger the particle radius, the greater the air adhesion resistance. It is more difficult for the particles to be adsorbed to the surface of the chip because a greater electrical force is required to overcome the adhesion resistance.

5. Conclusions

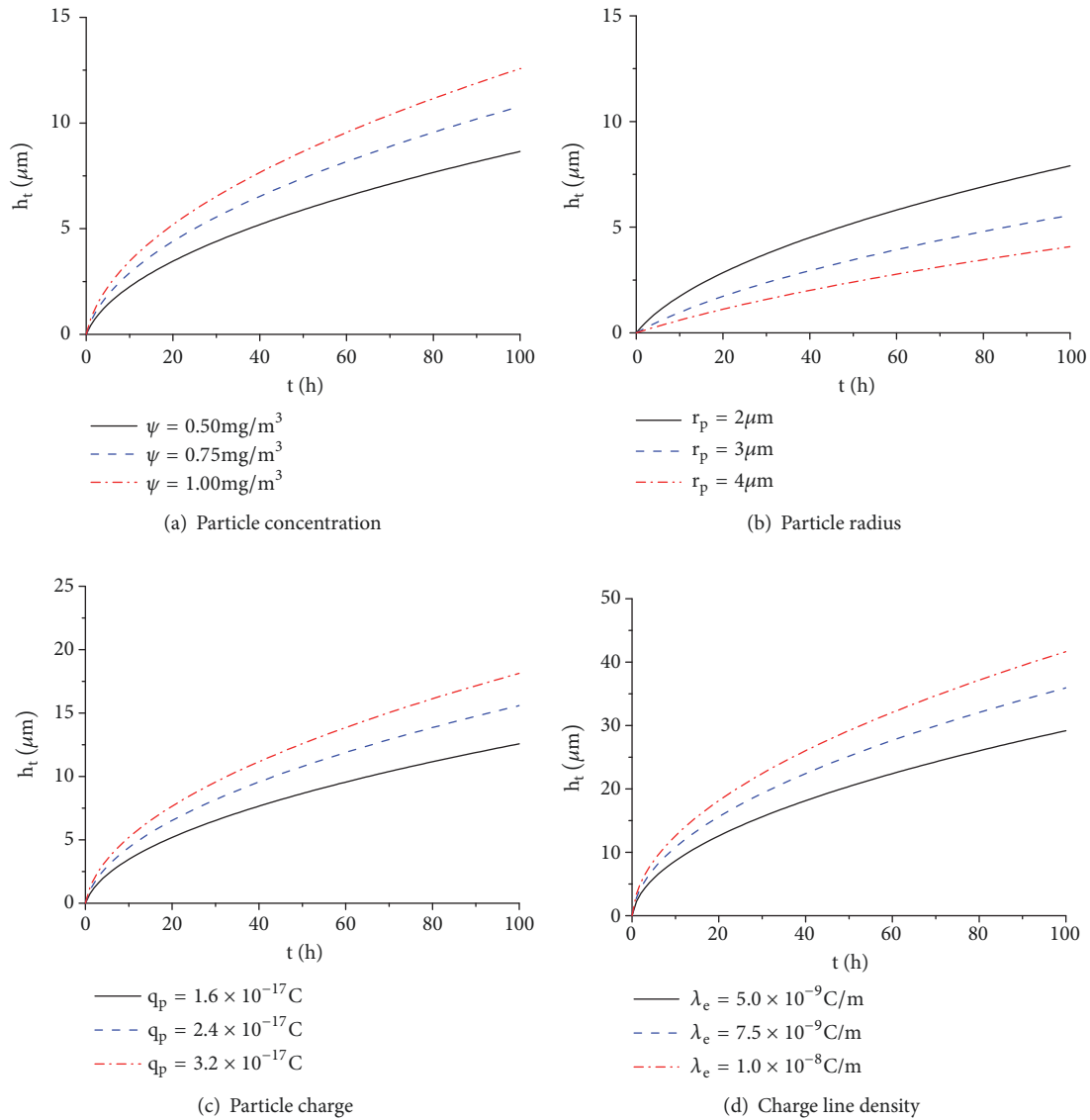(1) A theoretical model of contaminant adsorption accumulation with various affecting parameters on MEMS hot-film

FIGURE 14: Diagram of the effects of various factors on cumulative thickness.

gas flow sensor is established. From the model, it can be analyzed that the cumulative thickness of the particles increases while the growth rate declines over time. There are significant effects on the rate and thickness of contaminant accumulation with the particle concentration, the particle radius, the particle charge, and the electric field strength on the chip surface. The cumulative thickness of the particles increases along with the increase of the particle concentration, the particle charge, and the electric field strength on the chip surface but decreases along with the increase of the particle radius. Therefore, the rate and thickness of contaminant accumulation can be significantly reduced by decreasing the particle concentration, the particle charge, and the electric field strength on the chip surface, which can prolong the life of the sensor. These disciplines provide a theoretical basis for design and use of this type of sensor to control contamination at a minimum value.

(2) The cumulative thickness of the particles on the surface of the sensor chip and the variation of the sensor accuracy are obtained by the test. The cumulative thickness of the particles increases while the accuracy decreases over time. The measured data shows that when the gas flow rate is 5L/min, the cumulative thickness of the particles is $10.012 \mu m$ after the sensor works for 300 hours, and the related accuracy is reduced by 6.667%. The cumulative thickness is $14.801 \mu m$ after 600 hours working, and the related accuracy is reduced by 11.333%. The cumulative thickness is $18.331 \mu m$ after 900 hours working, and the related accuracy is reduced by 16%. The cumulative thickness is $20.921 \mu m$ after 1200 hours working, and the related accuracy is reduced by 20.667%. These results of the test fit those of the theoretical model.

(3) The test results indicate that the electrical force is the dominant cause of contaminant adsorption accumulation. By decreasing the electric field around the MEMS sensor surface

such as decreasing the voltage across the thin film resistor, the cumulative thickness of the particles can be effectively reduced. The test results also show that the contamination can be significantly reduced by increasing the filtration accuracy of the gas. This suggests that the accuracy of the sensor can be maintained for a long time under the condition that the filtration accuracy reaches 0.01μm.

Data Availability

The data used to support the findings of this study are available from the corresponding author.

Conflicts of Interest

The authors declare that they have no conflicts of interest.

Acknowledgments

References

[1] T. Glatzl, S. Cerimovic, H. Steiner et al., "Hot-film and calorimetric thermal air flow sensors realized with printed board technology," *Journal of Sensors and Sensor Systems*, vol. 5, no. 2, pp. 283–291, 2016.

[2] S. Cerimovic, A. Talic, R. Beigelbeck et al., "Bidirectional micromachined flow sensor featuring a hot film made of amorphous germanium," *Measurement Science & Technology*, vol. 24, no. 8, Article ID 084002, 2013.

[3] V. Balakrishnan, T. Dinh, H.-P. Phan, D. V. Dao, and N.-T. Nguyen, "Highly sensitive 3C-SiC on glass based thermal flow sensor realized using MEMS technology," *Sensors and Actuators A: Physical*, vol. 279, pp. 293–305, 2018.

[4] R. H. Ma, "A novel design of vehicle intake system detection based-on hot-film air flow meter sensors," *Journal of Engineering & Applied Sciences*, vol. 6, no. 1, pp. 43–48, 2011.

[5] W. Liu and L. F. Zhao, "Study on the dynamic characteristics of hot-film flow sensor based on the sampling air channel," *Applied Mechanics and Materials*, vol. 494-495, pp. 197–200, 2014.

[6] K. Grimm, A. Tonnesmann, and S. Nigrin, "Combustion engine waste gas mass flow sensor with a hot film anemometer, European, EP20110194555," 2013.

[7] S. E. Muldoon, M. Kowalczyk, and J. Shen, "Vehicle fault diagnostics using a sensor fusion approach," in *Proceedings of the First IEEE International Conference on Sensors - IEEE Sensors 2002*, vol. 2, pp. 1591–1596, USA, June 2002.

[8] M. Fleischer and M. Lehmann, *Solid State Gas Sensors - Industrial Application*, Springer, Berlin, Germany, 2012.

[9] T. Tille, "Automotive suitability of air quality gas sensors," *Sensors and Actuators B: Chemical*, vol. 170, pp. 40–44, 2012.

[10] B. Sam, "Successful MAF sensor diagnosis," *Motor*, vol. 7, pp. 28–36, 2006.

[11] S. Sekine, "Fault diagnosis apparatus for airflow meter," US, 13/642348, 2015.

[12] Q. Ahmed, A. I. Bhatti, and M. Iqbal, "Virtual sensors for automotive engine sensors fault diagnosis in second-order

[13] C. Xu, X. Guo, H. Jiang, S. Liu, and W. Cao, "Analysis of measurement reliability of hot-film air flow sensor influenced by air contaminant," in *Proceedings of the Electronic Components & Technology Conference*, vol. 4, pp. 2270–2276, 2015.

[14] I. Komorska and Z. Wółczyński, "Fault diagnostics of air intake system of the internal combustion engine," in *Proceedings of the International Congress on Technical Diagnostic*, vol. 10 of *Applied Condition Monitoring*, pp. 91–100, Springer International Publishing, 2016.

[15] H. Hecht, U. Konzelmann, and T. Schulz, "Sensor chip with additional heating element, method for preventing a sensor chip from being soiled, and use of an additional heating element on a sensor chip," US, 2003/0154807A1, 2003.

[16] B. Opitz, H. Hecht, U. Wagner, C. Gmelin, and K. Reymann, "Hot-film air-mass meter having a flow separating element," US, 2011/0036157 Al, 2011.

[17] C. Yuan, Z. Sun, X. Li, and Z. Guo, "Experimental study of particle deposition on thermal gas flow sensor," in *Proceedings of the 23rd International Conference on Mechatronics and Machine Vision in Practice, M2VIP 2016*, pp. 1–5, China, November 2016.

[18] Y. Shen, Z. Sun, C. Yuan, and X. Li, "Simulation about contamination influence of calorimetric flow sensor on measurement accuracy," in *Proceedings of the 8th IEEE International Conference on Cybernetics and Intelligent Systems, CIS 2017 and IEEE Conference on Robotics, Automation and Mechatronics, RAM 2017*, pp. 452–457, China, November 2017.

[19] A. Guha, "Transport and deposition of particles in turbulent and laminar flow," *Annual review of fluid mechanics*, vol. 40, no. 1, pp. 311–341, 2008.

[20] C. D. Dritselis, "Numerical study of particle deposition in a turbulent channel flow with transverse roughness elements on one wall," *International Journal of Multiphase Flow*, vol. 91, pp. 1–18, 2017.

[21] E. Rabinovich and H. Kalman, "Incipient motion of individual particles in horizontal particle–fluid systems: B. Theoretical analysis," *Powder Technology*, vol. 192, no. 3, pp. 318–325, 2009.

[22] F. Zhou, S. Hu, Y. Liu, C. Liu, and T. Xia, "CFD-DEM simulation of the pneumatic conveying of fine particles through a horizontal slit," *Particuology*, vol. 16, pp. 196–205, 2014.

[23] C. Jin, I. Potts, and M. W. Reeks, "A simple stochastic quadrant model for the transport and deposition of particles in turbulent boundary layers," *Physics of Fluids*, vol. 27, no. 5, article no 053305, 2015.

[24] P. Bunchatheeravate, J. Curtis, Y. Fujii, and S. Matsusaka, "Prediction of particle charging in a dilute pneumatic conveying system," *AIChE Journal*, vol. 59, no. 7, pp. 2308–2316, 2013.

[25] D. Desideri, M. Guarnieri, and E. Poli, "MV line electric field evaluation near a concrete pole," *IEEE Transactions on Magnetics*, vol. 40, no. 2, pp. 718–721, 2004.

[26] Y. Yamamoto and T. Okawa, "Numerical study of particle concentration effect on deposition characteristics in turbulent pipe flows," *Journal of Nuclear Science and Technology*, vol. 47, no. 10, pp. 945–952, 2010.

[27] P. Görner, X. Simon, D. Bémer, and G. Lidén, "Workplace aerosol mass concentration measurement using optical particle counters," *Journal of Environmental Monitoring*, vol. 14, no. 2, pp. 420–428, 2012.

[28] K. Ehara, K. Takahata, and M. Koike, "Absolute mass and size measurement of monodisperse particles using a modified

millikan's method: part II—application of electro-gravitational aerosol balance to polystyrene latex particles of 100 nm to 1 μm in average diameter," *Aerosol Science and Technology*, vol. 40, no. 7, pp. 521–535, 2006.